Applied Surface Science 463 (2019) 907–917

Contents lists available at ScienceDirect

Applied Surface Science

journal homepage: www.elsevier.com/locate/apsusc

Full Length Article

Geometry, electronic structure, morphology, and photoluminescence emissions of $BaW_{1-x}Mo_xO_4$ (x = 0, 0.25, 0.50, 0.75, and 1) solid solutions: Theory and experiment in concert

Marisa Carvalho Oliveira[a,b], Juan Andrés[a], Lourdes Gracia[c,*], Michelle Suzane M.P. de Oliveira[d], Jose Manuel R. Mercury[d], Elson Longo[b], Içamira Costa Nogueira[e]

[a] Departamento de Química Física y Analítica, Universitat Jaume I, 12071 Castelló de la Plana, Spain
[b] CDMF-UFSCar, Universidade Federal de São Carlos, P.O. Box 676, 13565-905 São Carlos, SP, Brazil
[c] Departamento de Química Física, Universitat de València, 46100 Burjassot, Spain
[d] PPGEM-IFMA, Instituto Federal do Maranhão, CEP 65030-005 São Luís, MA, Brazil
[e] Departamento de Física, UFAM, 3000-Japiim, Manaus, AM 69077-000, Brazil

ARTICLE INFO

Keywords:
$BaW_{1-x}Mo_xO_4$ solid solutions
DFT
Photoluminescence
Morphology
Co-precipitation

ABSTRACT

The design of a solid solution with tunable electro-optical properties and multifunctionality is a promising strategy for developing novel materials. In this work, $BaW_{1-x}Mo_xO_4$ (x = 0, 0.25, 0.5, 0.75, and 1) solid solutions have been successfully prepared for the first time by a co-precipitation method. Their crystal structure and phase composition were determined by X-ray diffraction and Rietveld refinements. Fourier transform infrared and micro Raman spectroscopy in combination with field-emission scanning electron microscopy (FE-SEM) were used to describe the microstructures and chemical compositions of the synthesized materials. The influence of chemical composition on morphology and photoluminescence (PL) emission has been analyzed. The geometry, electronic structures, and morphologies of $BaW_{1-x}Mo_xO_4$ (x = 0, 0.25, 0.5, 0.75, and 1) solid solutions were investigated by first-principles quantum-mechanical calculations based on the density functional theory. By using Wulff construction and the values of the surface energies for the (1 1 2), (0 0 1), (1 1 0), (1 0 1), (1 0 0), and (1 1 1) crystal faces, a complete map of the available morphologies for the $BaW_{1-x}Mo_xO_4$ solid solutions was obtained. These results show a qualitative agreement between the experimental morphologies obtained using the FE-SEM images and the computational models. The substitution of W^{6+} by Mo^{6+} enhances the electron-transfer process due to a stronger Mo(4d)-O(2p) hybridization compared to W(5d)-O(2p) for the W/Mo-O superficial bonds, and is responsible for the change in morphology from $BaWO_4$ to $BaMoO_4$. Such a fundamental study, which combines multiple experimental methods and first-principles calculations, has provided valuable insight into obtaining a basic understanding of the local structures, bonding, morphologies, band gaps, and electronic and optical properties of the $BaW_{1-x}Mo_xO_4$ (x = 0, 0.25, 0.5, 0.75, and 1) solid solutions.

1. Introduction

Alkaline earth molybdate and tungstate ($AMoO_4$ and AWO_4, A = Ba, Sr, or Ca) are inorganic compounds having the scheelite-type ABO_4 structure, and exhibit interesting properties for a wide range of applications such as scintillators, luminescent materials, electro-optical devices, and catalysts [1–5].

From a structural point of view, in the tetragonal scheelite structure (space group I41/a), each hexavalent metal cation, Mo^{6+} or W^{6+}, is tetrahedrally coordinated to four oxygen anions, yielding $[MoO_4]$ or $[WO_4]$ clusters. The alkaline earth bivalent metal cations, A^{2+}, are located between these tetrahedral clusters, forming an eightfold coordination with the oxygen anions, i.e., $[AO_8]$ clusters [6] or $[MoO_4]$/$[WO_4]$ clusters being the building blocks of their 3-D structures. The versatility of this family of complex oxide crystals is owing to the fact that their physical and chemical properties depend on their composition, which in turn allows the tuning of the final properties by changing the chemical composition. Very recently, L. Liu et al. [7] have obtained different morphologies by adjusting the relative concentrations of solute, water, and ethanol, while the mechanisms through which these morphologies were formed have been analyzed by using *in situ* scanning electron microscopy and atomic force microscopy.

* Corresponding author.
E-mail address: lourdes.gracia@uv.es (L. Gracia).

https://doi.org/10.1016/j.apsusc.2018.08.146
Received 10 May 2018; Received in revised form 25 July 2018; Accepted 18 August 2018
Available online 24 August 2018

Our group has been engaged in a research project devoted to the study of the structural, morphological, and optical properties of $BaWO_4$ [6] and $BaMoO_4$ [8] microcrystals by using a combination of theoretical calculations and experimental techniques [9]. As an extension of these studies, in this work, we focus our attention on $BaW_{1-x}Mo_xO_4$ solid solutions, in which both $BaWO_4$ and $BaMoO_4$ have the scheelite structure. When the W^{6+} cations in $BaWO_4$ are partially replaced by the Mo^{6+} cations, the formation of a $BaW_{1-x}Mo_xO_4$ solid solution is expected, and its structural, electronic, and optical properties can be tailored over a broad range, opening the door to finding new materials that can exhibit a wide range of technologically relevant properties. Recently, Bouzidi et al. [10] have prepared $BaW_{1-x}Mo_xO_4$ solid solutions (x = 0.00, 0.05, 0.10, 0.15, and 0.20) by a solid state reaction method, while Vidya et al. [11] have prepared $AMo_{0.5}W_{0.5}O_4$ (where A = Ba, Sr, or Ca) by a single-step modified combustion technique.

Based on the above considerations, in this work, we seek to fulfill a four-fold objective. The first is to report, for the first time, the synthesis of novel $BaW_{1-x}Mo_xO_4$ (x = 0, 0.25, 0.5, 0.75, and 1) solid solutions by employing a co-precipitation method. This synthesis method has received special attention due to allow the formation of oxides with high degree of crystallinity and easy dispersion in aqueous medium, reduce the reaction times, low synthesis temperatures, excellent control of reaction parameters, excellent control size and morphology of product, and enhance product purity or material properties [12–16]. Secondly, X-ray diffraction (XRD), Fourier transform infrared (FT-IR), and micro Raman (MR) spectroscopy, in combination with field-emission scanning electron microscopy (FE-SEM) and Rietveld refinements, were employed to characterize the samples and determine the effect of their chemical composition on the morphology and photoluminescence (PL) emissions. The third aim is to investigate the geometry, electronic structure, and properties of $BaW_{1-x}Mo_xO_4$ using the density functional theory (DFT). The fourth aim is to apply a joint experimental and theoretical strategy developed by us to obtain a complete map of the morphologies available for the $BaW_{1-x}Mo_xO_4$ solid solutions. Based on these results, we hope to understand how the different surfaces change their energies throughout the synthesis process, and propose a mechanism by which the experimental and theoretical morphologies of the $BaW_{1-x}Mo_xO_4$ solid solutions match. We believe that these novel results are of significant relevance, since they may inspire the efficient synthesis of these and related molybdate/tungstate solid solutions and provide critical information to expand our fundamental understanding of the effect of substitution of W by Mo in these compounds.

This paper contains three more sections. The next section is the experimental section (synthesis and characterization), where the computational details are given. In section three, the results are presented and discussed. The main conclusions are summarized in the fourth and final section.

2. Experimental procedures

2.1. Synthesis

$BaW_{1-x}Mo_xO_4$ (x = 0, 0.25, 0.50, 0.75, and 1) solid solutions were synthesized by a co-precipitation method at 80 °C. Sodium tungstate dihydrate ($Na_2WO_4{\cdot}2H_2O$, Stream Chemical, 99.5%, 1×10^{-3} mol) and sodium molybdate dihydrate ($Na_2MoO_4{\cdot}2H_2O$, Stream Chemical, 99.95%, 1×10^{-3} mol) were dissolved in 50 mL of distilled water at 80 °C by vigorous stirring. Then, 1×10^{-3} mol of barium nitrate ($Ba(NO_3)_2$, Sigma-Aldrich, 99%), solubilized in 50 mL of distilled water at 80 °C, was added to the previously mentioned solution. The solution was maintained at 80 °C until the $BaW_{1-x}Mo_xO_4$ crystals precipitated. This precipitate was washed with distilled water several times, collected, and dried in a conventional furnace at 50 °C for 8 h.

2.2. Characterization

To determine the phase composition and crystal structure of the as-synthesized $BaW_{1-x}Mo_xO_4$ (x = 0, 0.25, 0.50, 0.75, and 1) crystals, X-ray powder diffraction (XRD) was employed in combination with Rietveld refinements [17] and the General Structure Analysis System program [18]. The measurements were carried out using a D/MAX/2500PC diffractometer (Rigaku, Japan) operating at 40 kV and 150 mA with Cu Kα radiation (λ = 1.5406A) in the 2θ range 10° to 110° at a scan rate of 0.02°/min. The diffraction peak profiles were adjusted using the Thompson–Cox–Hastings pseudo-Voigt (pV-TCH) function and an asymmetry function described by Finger et al. [19]. The background was corrected using a Chebyshev polynomial of the first order. The strain anisotropy broadening was corrected using the phenomenological model described by Stephens [20]. The high-quality powder diffraction data in combination with the Rietveld method allowed the refinement of a structural model (atomic coordinates, site occupancies, and atomic displacement parameters), as well as the profile parameters (lattice constants, peak shape, sample height, and background).

The morphologies of the particles were observed with a field-emission scanning electron microscope, model InspectF50 (FEI Company, Hillsboro, USA), operated at 15 kV. The Fourier transform infrared spectroscopy (FT-IR) patterns were recorded in the range 250–1100 cm^{-1} using KBr pellets as a reference in a Bomen-Michelson spectrophotometer in the transmittance mode (model MB-102). Micro Raman (MR) spectroscopy was conducted on a Horiba Jobin-Yvon (Japan) spectrometer coupled to a charge-coupled device detector and Ar-ion laser (MellesGriot, United States) operating at 514.5 nm with a maximum power of 200 mW. The spectra were measured in the range 48–1100 cm^{-1}. The PL spectra were measured with a Monospec 27 monochromator (Thermal Jarrel Ash, United States) coupled to a R446 photomultiplier (Hamamatsu Photonics, Japan). A Kr ion laser (Coherent Innova 200 K, United States) (λ = 350 nm) was used as the excitation source. The incident laser beam power on the sample was maintained at 15 mW. All the measurements were performed at room temperature.

2.3. Computational details

Quantum-mechanical calculations using DFT at the B3LYP hybrid functional level [21,22] have been carried out by means of the CRYSTAL14 computer code [23]. This method has been successfully employed in various studies of the bulk and surface electronic and structural properties of perovskite [24,25], molybdate [26,27,8], and tungstate based materials [28–30,6], as well as Ag_2CrO_4 [31], and $LaVO_4$ [32].

The atomic centers were described using pseudopotential basis sets for the Mo [33] atom and large-core effective core potentials derived by Hay and Wadt, modified by Cora et al. [34] for the W atom; while the O [35] and Ba [36] atoms were described by the standard all-electron-basis sets (6-31G* basis set).

The irreducible edge of the Brillouin zones was sampled using the Monkhorst–Pack method [37] at different k-point grids according to the system size. The thresholds controlling the accuracy of the calculation of the Coulomb and exchange integrals were set to 10^{-8} (ITOL1 to ITOL4) and 10^{-14} (ITOL5), which assures a convergence in total energy better than 10^{-7} a.u., whereas the percentage of Fock/Kohn–Sham matrix mixing was set to 40 (IPMIX = 40) for the calculation of the equilibrium geometries and electronic properties of the $BaW_{1-x}Mo_xO_4$ structures.

The initial cell and atomic position parameters used in the optimization process were taken from the results of Rietveld refinements of $BaWO_4$ and $BaMoO_4$. The scheelite structure is characterized by barium atoms bonded to eight oxygen atoms, resulting in [BaO_8] bisdisphenoid

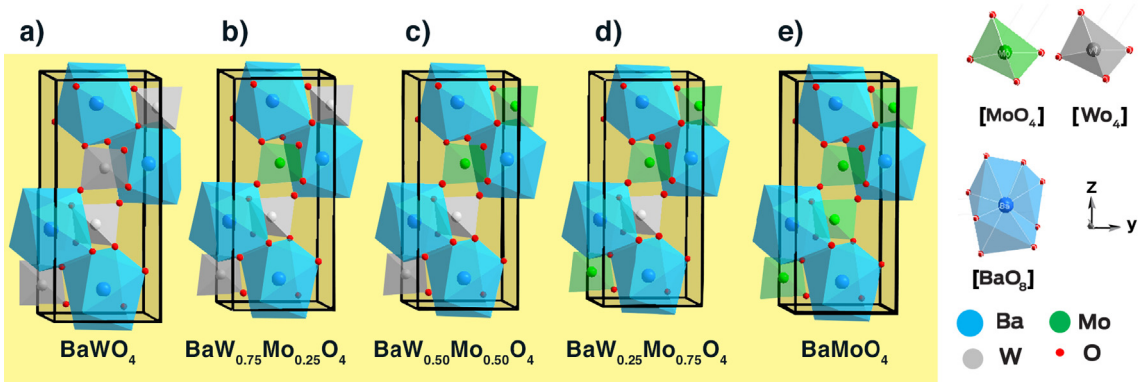

Fig. 1. Unit cell representation of $BaW_{1-x}Mo_xO_4$ crystals: (a) x = 0, (b) x = 0.25, (c) x = 0.50, (d) x = 0.75, and (e) x = 1. The constituent clusters: $[MoO_4]$, $[WO_4]$ and $[BaO_8]$ are depicted.

clusters, and the molybdenum or tungsten atoms coordinated to four oxygen atoms in a tetrahedral configuration, i.e., forming $[MoO_4]$ or $[WO_4]$ clusters.

The scheelite $BaWO_4$ conventional unit cell containing 24 atoms is showed in Fig. 1(a). There are four W atoms in the structure generated from the *4a* Wyckoff position by symmetry operations.

In order to investigate the energetics of the Mo^{6+} distribution, several representative cells were generated, differing in the positions of the Mo^{6+} cations. In the most stable arrangement, the Mo^{6+} ions lie far apart, and the corresponding structures for $BaW_{1-x}Mo_xO_4$ (x = 0.25, 0.5, 0.75, and 1) are depicted in Fig. 1(b), (c), (d), and (e), respectively.

The slab models containing 4, 4, 4, 8, 4, and 4 molecular units for the (0 0 1), (1 0 1), (1 1 0), (1 0 0), (1 1 1), and (1 1 2)) crystal faces of $BaW_{1-x}Mo_xO_4$ (x = 0, 0.25, 0.50, 0.75, and 1), respectively, were used in the calculations, and are shown in Fig. 2. These surfaces were modeled using symmetrical slabs (with respect to the mirror plane), and all of them were terminated with the O planes. After the corresponding optimization process and thickness convergence tests, the resulting slab models consisted of four molecular units containing 24 ions on the (0 0 1), (1 0 1), (1 1 0), (1 1 1), and (1 1 2) crystal faces, while the (1 0 0) crystal face was modeled containing 48 ions, considering a thickness of the slab not lower than 7 Å.

The surface calculations were based on the equilibrium morphology of a crystal predicted by the classic Wulff construction, which minimizes the total surface energy at a fixed volume, providing a simple correlation between the surface energy (E_{surf}) of the (*hkl*) plane and its distance r_{hkl} in the normal direction from the center of the crystallite [38]. The surface energy (E_{surf}) of each crystal face is defined as the total energy per repeating cell of the slab (E_{slab}) minus the total energy of the perfect crystal per molecular unit for each percentage of solid

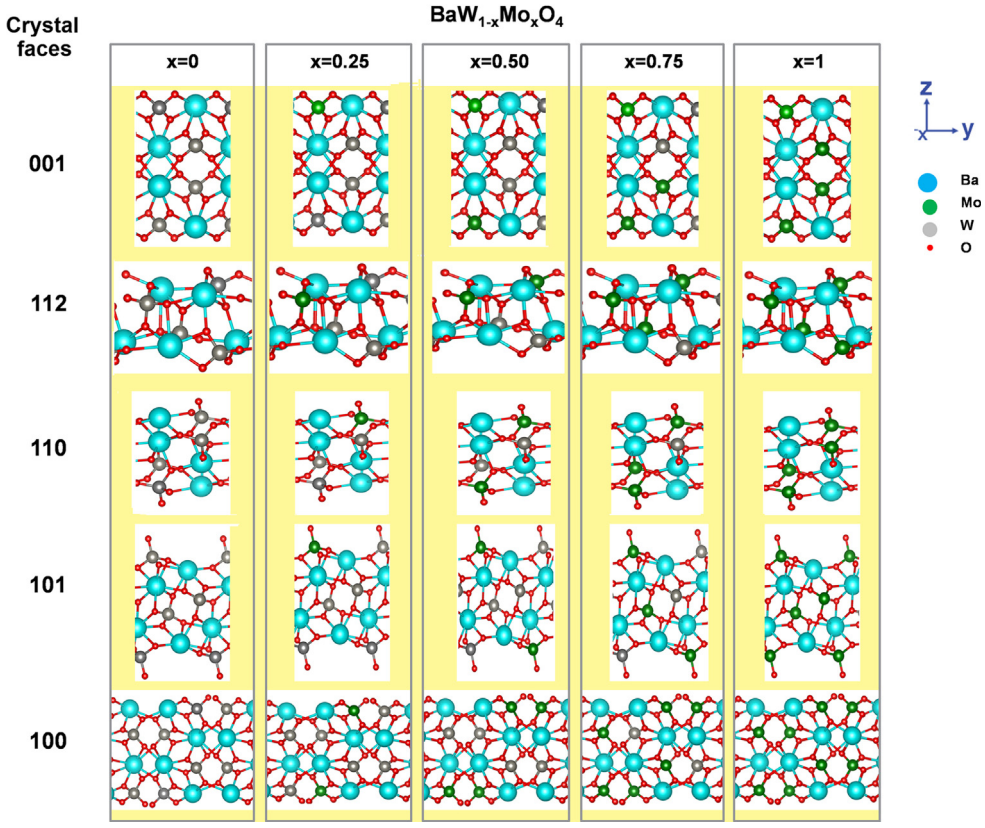

Fig. 2. Schematic representations of the different crystal faces of $BaW_{1-x}Mo_xO_4$ (x = 0, 0.25, 0.50, 0.75, and 1) solid solutions.

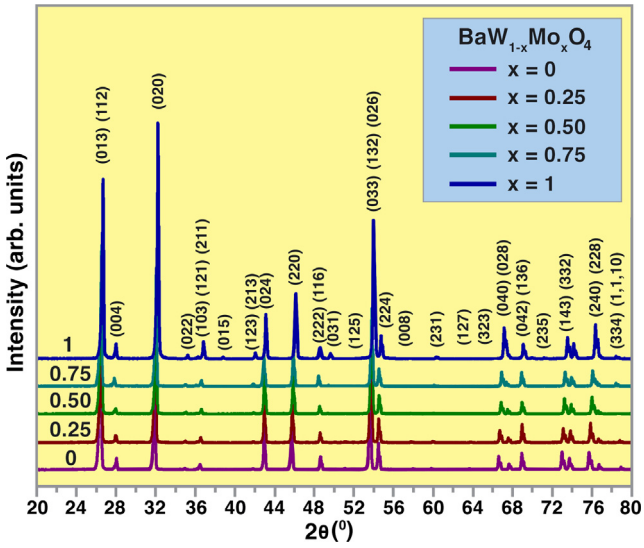

Fig. 3. X-ray diffraction patterns of $BaW_{1-x}Mo_xO_4$ (x = 0, 0.25, 0.50, 0.75, and 1) crystals.

solution, i.e., 0, 25, 50, 75, and 100% (E_{bulk}) multiplied by the number of molecular units on the surface (N) and divided by the surface area, A, per repeating cell of the two sides of the slab, as shown in Eq. (1).

$$E_{suf} = \frac{1}{2A}(E_{slab} - NE_{bulk}) \quad (1)$$

3. Results and discussion

3.1. X-ray diffraction and Rietveld refinements

The structural study of the $BaW_{1-x}Mo_xO_4$ (x = 0, 0.25, 0.50, 0.75, and 1) solid solutions was performed by means of XRD (Fig. 3) and Rietveld refinements (Fig. S1).

Supplementary data associated with this article can be found, in the online version, at https://doi.org/10.1016/j.apsusc.2018.08.146.

An analysis of the XRD patterns displayed in Fig. 3 shows that all the peaks can be indexed perfectly to a scheelite-type-tetragonal structure, with the space group symmetry I41/a and four molecular formula units per unit cell (Z = 4) [39]. The XRD peak patterns and Rietveld refinement plots of these crystals show good agreement between the experimentally observed XRD patterns and the theoretically fitted results (see Fig. S1(a-c)). The XRD patterns illustrate that all the diffraction peaks for the $Ba(W_{1-x}Mo_x)O_4$ crystals are monophasic, without the presence of secondary phases. Thus, it was proved that the substitution of W^{6+} by Mo^{6+} in the $BaWO_4$ crystal lattice forms $Ba(W_{1-x}Mo_x)O_4$ solid solutions. The occupation sites of W^{6+} and Mo^{6+} for each solid solution in the crystal lattice, as calculated by the Rietveld refinements, are presented in Table 1. The good quality for the structural refinements is evidenced by the low deviations of the statistical parameters (R_{wp}, R_p, R_{Bragg} and χ^2). These parameters are listed in Table 1 and suggest that the measured diffraction patterns are in good agreement with the ICSD entry No. 155511 [39].

For comparison, first-principles calculations were used to determine the lattice parameters (Table 1) and atomic coordinates (Table S1) of the oxygen anions. These results are in good agreement with previous experimental observations. An analysis of the results shows that the substitution of W^{6+} by Mo^{6+} induces variations in the atomic coordinates of the oxygen atoms (see Table S1), indicating the existence of structural and electronic distortions in the $[WO_4]$, $[MoO_4]$, and $[BaO_8]$ clusters, as well as changes in the lattice parameters and a reduction in the unit cell volume.

Table 1
Lattice parameters, unit cell volume, and statistical parameters of the $BaW_{1-x}Mo_xO_4$ (x = 0.25, 0.50, and 0.75) solid solutions obtained by Rietveld refinements and calculations.

Sample $BaW_{1-x}Mo_xO_4$	Lattice parameters				
	Cell volume $(Å)^3$	α = β = γ = 90°			
		Experimental		Theoretical	
		a = b (Å)	c (Å)	a = b (Å)	c (Å)
x = 0	401.42	5.614(9)	12.732(6)	5.581(4)	12.412(6)
x = 0.25	401.27	5.608(0)	12.759(0)	5.588(1)	12.445(0)
x = 0.50	400.81	5.599(3)	12.783(9)	5.594(1)	12.477(8)
x = 0.75	400.53	5.591(4)	12.811(0)	5.599(7)	12.519(2)
x = 1	399.83	5.583(0)	12.827(0)	5.602(6)	12.574(6)
ICSD 155511 $BaWO_4$	398.48	5.603(4)	12.693(7)		

$R_{Bragg}(\%) = 6.95^a, 6.83^b, 6.29^c$; $\chi^2(\%) = 1.14^a, 1.20^b, 1.27^c$; $R_{wp}(\%) = 13.64^a, 14.85^b, 16.28^c$; $R_p(\%) = 8.71^a, 9.94^b, 11.07^c$.

3.2. Vibrational analysis

Molybdate and tungstate crystals with the scheelite-type tetragonal structure present 26 different vibration modes: $\Gamma(\text{Raman + infrared}) = 3A_g + 5_{Au} + 5_{Bg} + 3_{Bu} + 5_{Eg} + 5_{Eu}$, with A_g, B_g, and E_g being the Raman-active modes. Furthermore, the odd modes (A_u and E_u) are the active vibrational modes in the infrared spectra [40]. The experimental/theoretical spectra are shown in Fig. 4(a–f).

The Raman spectra of the scheelite structures can be interpreted in terms of the modes of the $[MO_4]^{2-}$ (M = Mo or W) tetrahedra, which can be considered as the constituent units in the structures. Thus, these modes can be classified either as internal vibrations (the $[MO_4]^{2-}$ (M = Mo or W) center of mass does not move) or as external vibrations (motion of the Ba^{2+} cations and the movements of the $[MO_4]^{2-}$ tetrahedra as rigid units). The corresponding representation for the tetrahedral symmetry is composed of four internal modes $\nu_1(A_1) + \nu_2(E) + \nu_4(F_2)$, one free rotation mode $\nu_{fr}(F_1)$, and one translation mode $\nu_3(F_2)$; however, only some of these modes are active in the IR spectrum, namely, ν_3, $\nu_4(F_2)$ [41].

In the FTIR spectrum of $BaW_{1-x}Mo_xO_4$ (x = 0.25, 0.50, and 0.75), the $3B_u$ vibrations are silent modes; one A_u and one E_u modes are acoustic vibrations. The experimental FTIR spectra are illustrated in Fig. S2. A metal-oxygen band in the MO_4^{2-} cluster (M = Mo and W) appears in the FTIR spectrum (see Fig. (S2)), corresponding to the internal modes indicated as the antisymmetric stretching ($\nu_3(F_2)$) vibrations at 811–830 cm^{-1} and the bending vibration ($\nu_4(F_2)$), observed as a strong band at about 380 cm^{-1}.

The experimental and calculated Raman-active modes are shown in Fig. 4(a–f), indicating the existence of a strong interaction between the ions, which arises from the stretching and bending vibrations of the shorter metal–oxygen bonds within the anionic groups [42]. A comparison between the relative positions of the Raman-active modes for the $BaW_{1-x}Mo_xO_4$ (x = 0.25, 0.50, and 0.75) solid solutions are shown in Fig. 4(b–f). DFT calculations using the B3LYP functional tend to overestimate the values of the vibrational frequencies; therefore, a scaling factor of 0.96 was used [43]. The calculations reveal the presence of three modes (A_g, E_g, and B_g, at approximately 452–375 cm^{-1}) not experimentally observed. A plausible explanation for this result can be that these modes have a very low intensity and are not easily detectable by experimental techniques.

Two high-frequency bands centered at 927 cm^{-1} for $BaWO_4$ and 894 cm^{-1} for $BaMoO_4$ are also present in $BaW_{1-x}Mo_xO_4$ (x = 0.25, 0.50, and 0.75) solid solutions, which correspond to intense peaks in the Raman (A_g) mode and are assigned to the symmetric stretching $\nu_1(A_1)$ of the bonds [←O ← M → O→] (M = Mo and W), while the two Raman

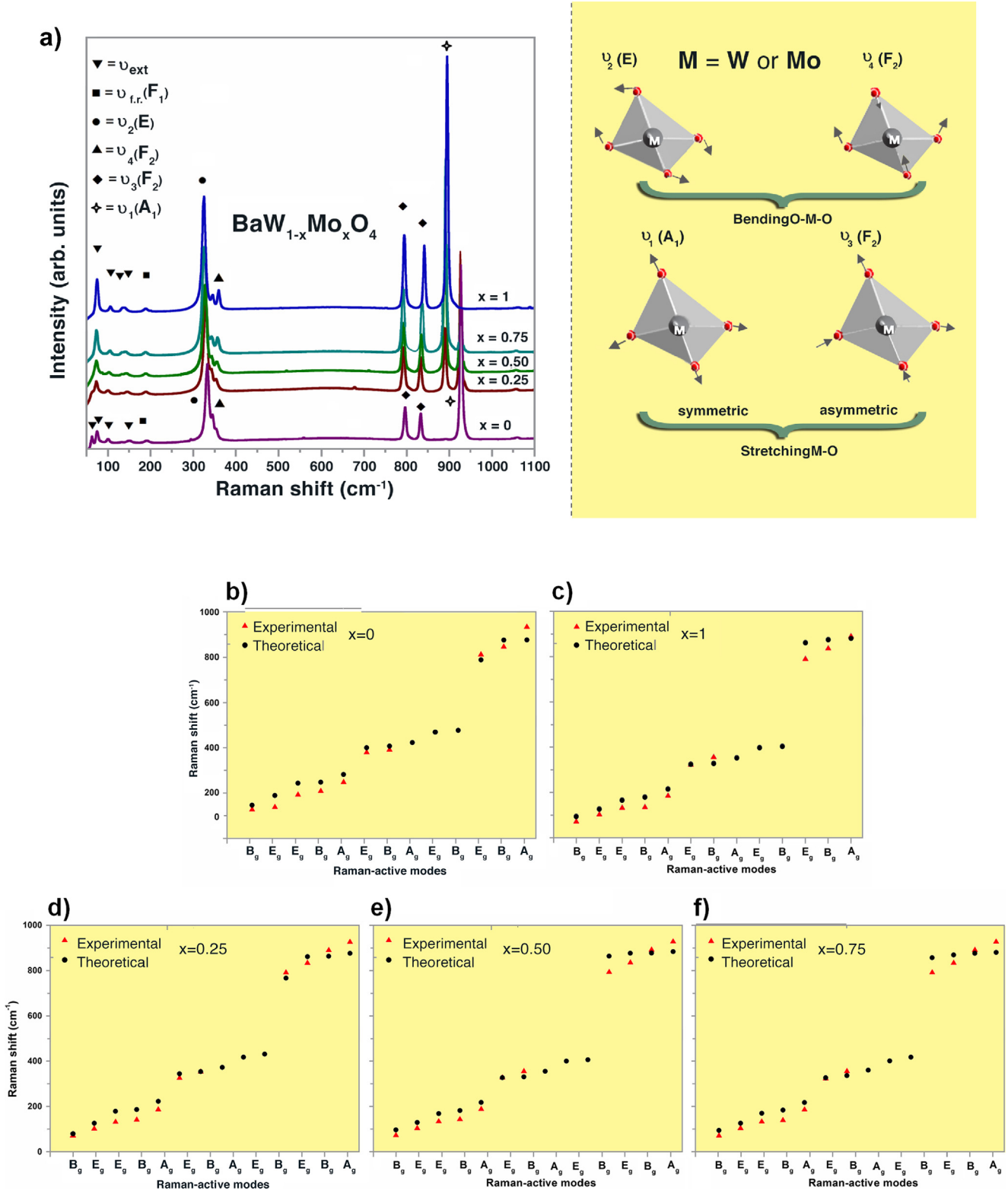

Fig. 4. MR spectra of $BaW_{1-x}Mo_xO_4$ (x = 0, 0.25, 0.50, 0.75, and 1) solid solutions. (a) experimental spectra. In (b) x = 0, (c) x = 1, (d) x = 0.25, (e) x = 0.50 and (f) x = 0.75, the calculated values are compared with the experimental Raman-active modes.

(B_g and E_g internal) modes at 836 and 792 cm^{-1} are attributed to the asymmetric stretching $\nu_3(F_2)$ of the bonds (→O → M → O→).

The peaks located at 357 and 324 cm^{-1} are assigned ($\nu_4(F_2)$, $\nu_2(E)$) to the rotational modes (E_g, B_g) as the bending modes. The free rotational $\nu_{fr}(F_1)$ mode at about 188 cm^{-1}, in addition to the external peaks (ν_{ext}) corresponding to the motions of MO_4^{2-} and Ba^{2+} are shown at approximately 74, 107, 126, and 143 cm^{-1}, which are assigned to rotational (A_g, E_g) and translational modes (B_g).

3.3. Photoluminescence emissions

The PL spectra of the $BaW_{1-x}Mo_xO_4$ (x = 0.25, 0.50, and 0.75) solid

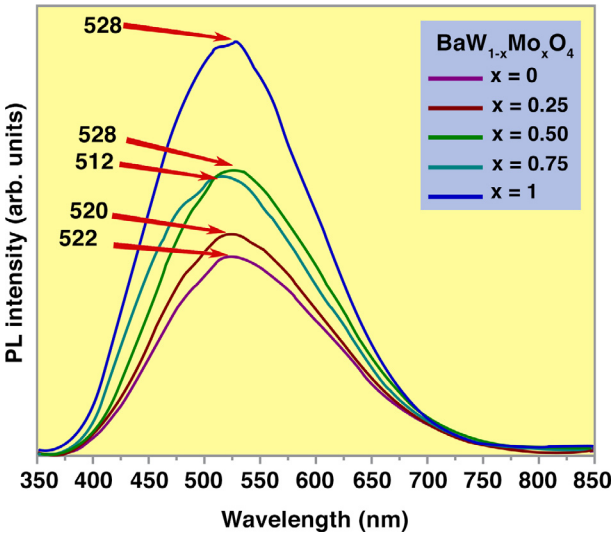

Fig. 5. PL spectra of $BaW_{1-x}Mo_xO_4$ (x = 0, 0.25, 0.50, 0.75, and 1) crystals.

solutions using the same excitation at 350 nm are depicted in Fig. 5.

All the compositions (x = 0, 0.25, 0.50, 0.75, and 1) exhibit PL emission peaks centered at 522, 520, 528, 512, and 528 nm, respectively. We note that the emission is attributed to the charge transfer in the $[MO_4]^{2-}$ (M = Mo and W) complex. The wide visible emission originates from the charge-transfer transition between the O 2p orbital and the empty d orbital of the $[MO_4]^{2-}$ (M = Mo and W) tetrahedral structure, with excitation energies located within the band gap [44,45], i.e., self-trapping electron states. The one ground state is $^1A_1$ and the four single excited states are $^1A(^1T_1)$, $^1E(^1T_1)$, $^1E(^1T_2)$, and $^1B(^1T_2)$ [46,47].

The PL curves shown in Fig. 5 represent a different type of electronic transition that can be associated with a specific structural arrangement of $[WO_4]$ or $[MoO_4]$ clusters, and can also be observed in the experimental results obtained from the Raman spectra that show two high-frequency bands at 927 cm^{-1} and 894 cm^{-1} for $BaWO_4$ and $BaMoO_4$, respectively, as well as for the $BaW_{1-x}Mo_xO_4$ (x = 0.25, 0.50, and 0.75) solid solution. In addition, we believe that the differences in the PL emission intensities presented in Fig. 5 are induced by the substitution of W^{+6} by Mo^{+6} as the $BaW_{1-x}Mo_xO_4$ (x = 0.25, 0.50, and 0.75) solid solutions form, which can be associated with the influence of the chemical composition and electronic transition, as discussed in the next section.

3.4. Electronic properties

The local coordination of the superficial Mo^{6+} and W^{6+} is fundamental for describing the order of stability of the different surfaces of the $BaW_{1-x}Mo_xO_4$ (x = 0, 0.25, 0.5, 0.75, and 1) solid solutions. The cleavage process associated with the slab model induces the presence of under-coordinated cations at the surface plane. Then, it is possible to find a relationship between the geometry, electronic structure, and surface energy values in order to discuss the order of stability of the investigated models.

We note that all the slabs expose the superficial $[BaO_6]$ or $[BaO_5]$ clusters. However, the (0 0 1), (1 1 2), (1 0 1), (1 1 0), and (1 0 0) crystal faces present $[MO_4]$ (M = Mo or W) clusters, while the (1 1 1) crystal face shows superficial $[MO_3]$ (M = Mo or W) clusters, implying the breaking of a M—O bond compared to the bulk compound. An analysis of both the (0 0 1) and (1 1 2) crystal faces reveals the presence of two-coordinated superficial O anions, Ba—O—M (M = Mo or W) on the (0 0 1) crystal face, while on the (1 1 2) crystal face, we observe the appearance of two types of superficial O anions with a coordination of one, O—M, or two, Ba—O—M (M = Mo or W). Then, the (0 0 1) crystal face exhibits just one dangling bond per exposed oxygen anion, while the (1 1 2) crystal face presents oxygen anions with the lowest coordination numbers.

Table 2
Calculated values of the surface energy, relaxation, and gap energy for each crystal face of $BaW_{1-x}Mo_xO_4$ solid solutions for x = 0, 0.25, 0.5, 0.75, and 1.

Crystal face	Mo percentage	$E_{surf}(J/m^2)$	Relaxation (%)	E_{gap}(eV)
(0 0 1)	0%	1.02	7	5.92
	25%	0.55		
	50%	0.54	14	5.97
	75%	0.54	20	5.69
	100%	0.99		
(1 1 2)	0%	0.92	5	6.14
	25%	0.65		
	50%	0.64	9	5.57
	75%	0.63	12	5.54
	100%	1.02		
(1 0 0)	0%	1.22	4	5.49
	25%	1.09		
	50%	1.09	8	5.48
	75%	1.08	10	5.33
	100%	1.17		
(1 1 0)	0%	1.10	4	6.15
	25%	0.80		
	50%	0.79	7	6.14
	75%	0.80	10	5.49
	100%	1.23		
(1 0 1)	0%	1.31	4	6.16
	25%	0.91		
	50%	0.89	8	6.21
	75%	0.90	12	5.31
	100%	1.34		
(1 1 1)	0%	2.06	1	
	25%	1.91		
	50%	1.89	1	Conductor
	75%	1.90	1	
	100%	2.23		

The calculated values of the surface energy, relaxation, and gap energy for the different crystal faces of the $BaW_{1-x}Mo_xO_4$ (x = 0, 0.25, 0.5, 0.75, and 1) solid solutions are presented in Table 2. The inversion in the stability order between the (0 0 1) and (1 1 2) crystal faces with respect to pure $BaWO_4$ can be associated with the inclusion of Mo^{6+} in the crystalline structure of $BaW_{1-x}Mo_xO_4$, inducing a stronger Mo(4d)—O(2p) hybridization compared to W(5d)—O(2p) for the superficial bonds that stabilize the dangling bond effect. This fact enhances the electron-transfer process on the surface plane, facilitated by the presence of the Mo^{6+} cation. Therefore, we can argue that the (0 0 1) crystal face becomes more stable than the (1 1 2) crystal face in $BaW_{0.75}Mo_{0.25}O_4$, $BaW_{0.5}Mo_{0.5}O_4$, $BaW_{0.25}Mo_{0.75}O_4$, and $BaMoO_4$ due to the smallest contribution of the dangling bond effect to the value of E_{surf}.

The calculated band structure and density of states (DOS) projected for the atoms and orbitals of $BaW_{0.5}Mo_{0.5}O_4$ corresponding to the (0 0 1), (1 0 1), (1 1 0), and (1 1 2) crystal faces are displayed in Fig. 6. An analysis of the band structure and projected DOS presented here shows that the band gap values (see Table 2) are in the range 0.1–0.8 eV, and depend significantly on the local coordination of both Mo^{6+} and W^{6+} at the different crystal faces. The main contribution to the valence band (VB) region is due to the 2p orbitals of the oxygen anions and a predominance of the dx^2-y^2 and dz^2 states of Mo^{6+} and W^{6+} found in the conduction band (CB) region.

In addition, theoretical methodology can contribute to an explanation for the optical properties, since a reduction in the band gap value is observed mainly in the cases of the (1 0 0) and (1 0 1) crystal faces. The density of states projected on the atoms as a function of layer position for the (1 0 0) and (1 0 1) crystal faces of the $BaW_{1-x}Mo_xO_4$ (x = 0.25,

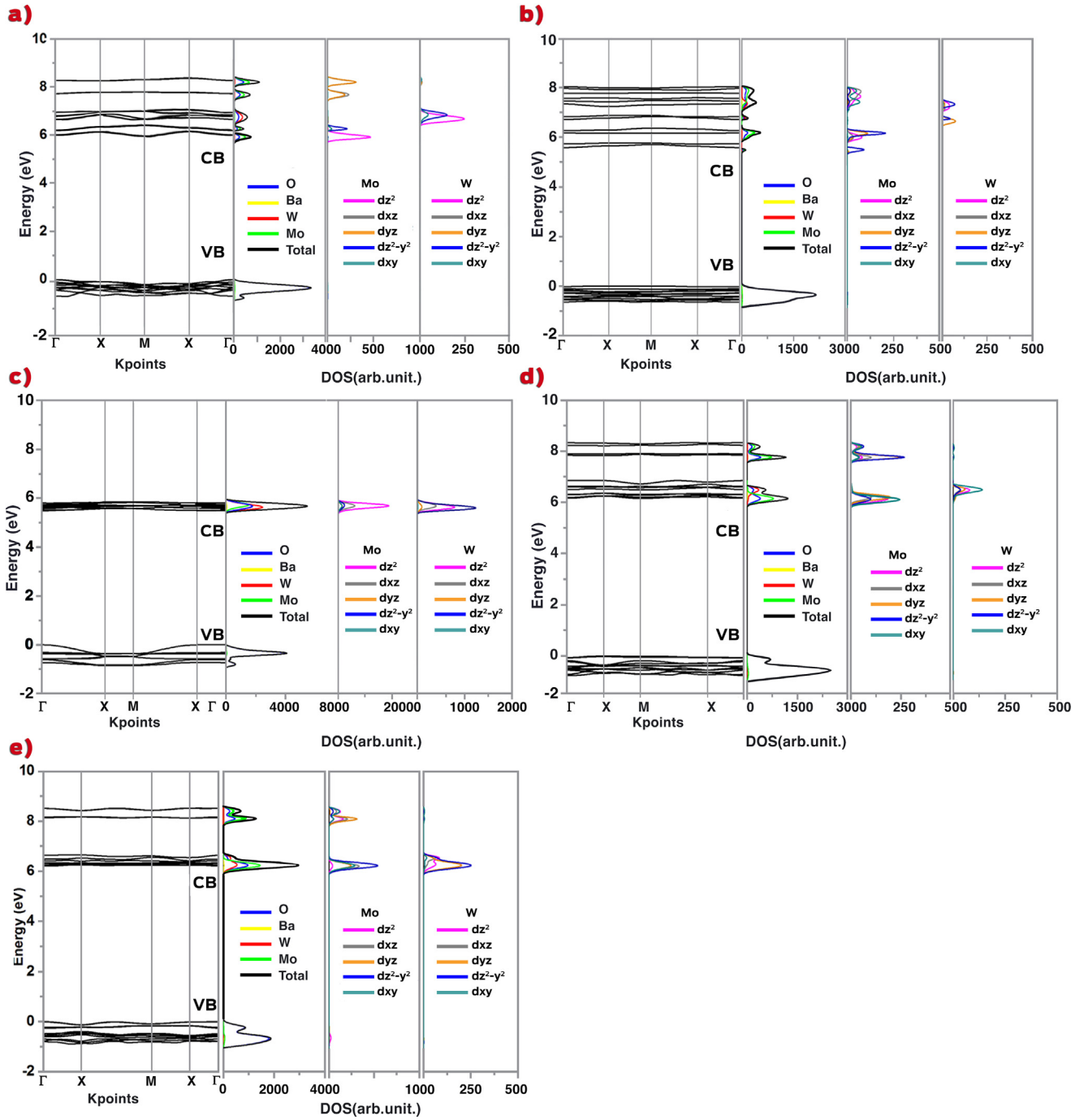

Fig. 6. The band structure and density of states projected on atoms and orbitals for (a) (0 0 1), (b) (1 1 2), (c) (1 0 0), (d) (1 1 0) and (e) (1 0 1) crystal faces at $BaW_{0.5}Mo_{0.5}O_4$.

0.50, and 0.75) solid solutions is presented in Fig. 7.

An analysis of Fig. 7 shows that for the (1 0 0) and (1 0 1) crystal faces the distribution of the energy levels of each layer of the $BaW_{1-x}Mo_xO_4$ (x = 0.25, 0.50, 0.75) solid solution is related to the electron transfer from the O anions to the d orbitals of Mo^{6+} or W^{6+}, which are the electronic transitions associated with the PL emissions. Furthermore, it was observed that the isoelectronic replacement of Mo^{6+} by W^{6+} perturbs the energy-level distribution in the vicinity of the band-gap region, narrowing the corresponding excitation energy, mainly for the CB, since the 4d valence orbitals of Mo^{6+} have a lower energy than those of W^{6+} (5d). However, the results show that both the metals contribute equally in the lower energy region of the CB, suggesting a competition for the electron trapping mechanism, i.e., the excited electrons from the O (2p) levels can be located in both the $[MoO_4]$ and $[WO_4]$ clusters, which could be related to the non-linear wavelength displacement observed in the experimental PL emissions (Fig. 5).

3.5. Morphology

The conventional approach to the quantitative study of changes in morphology is by applying the Wulff construction using the calculated surface energies [38]. In previous publications, $BaWO_4$ and $BaMoO_4$ have been described in detail, and it was noted that the ideal morphology for the $BaWO_4$ and $BaMoO_4$ systems is defined mainly by their (1 1 2), (0 0 1), and (1 0 0) crystal faces [8], as presented in other scheelite crystals [48].

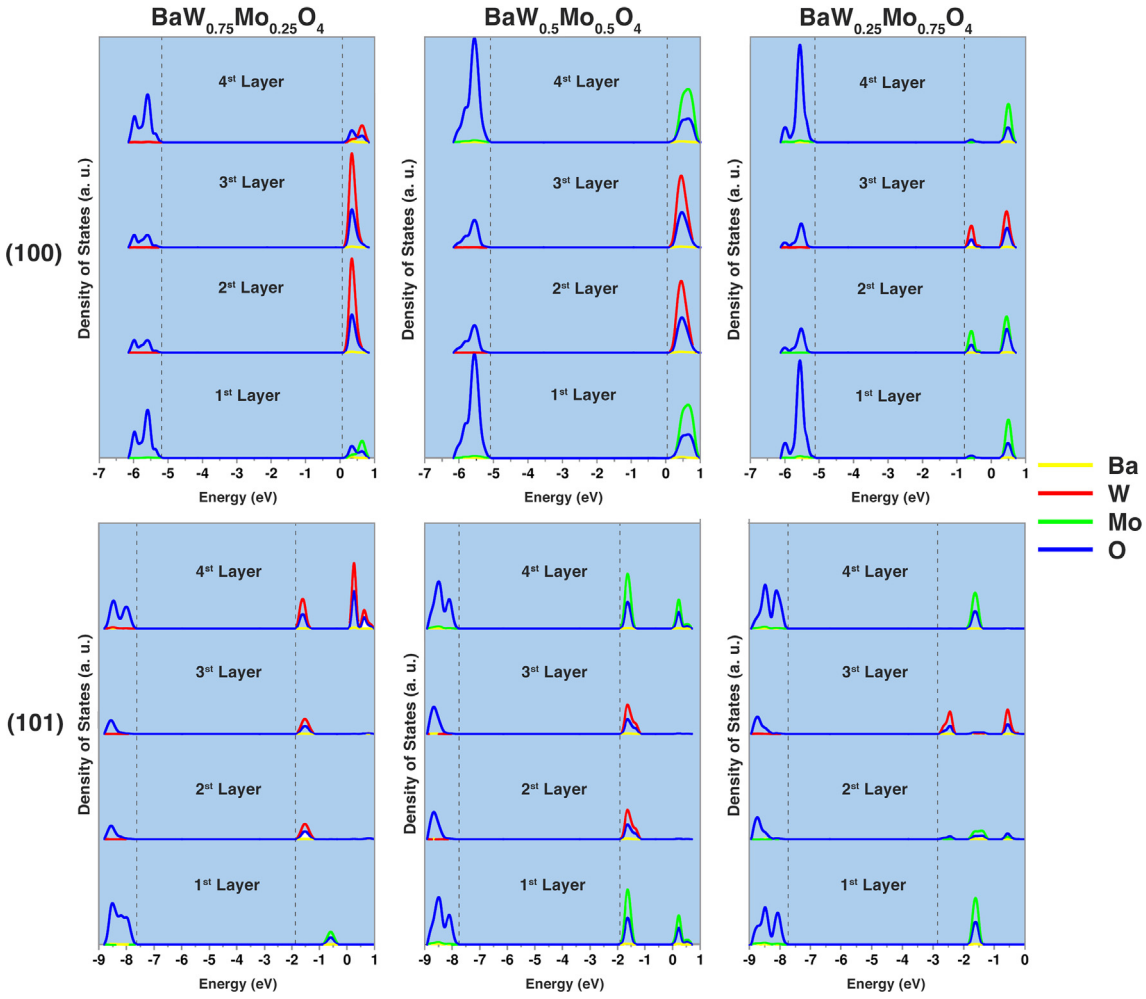

Fig. 7. Density of states projected on atoms as a function of layer position at (1 0 0) and (1 0 1) crystal faces.

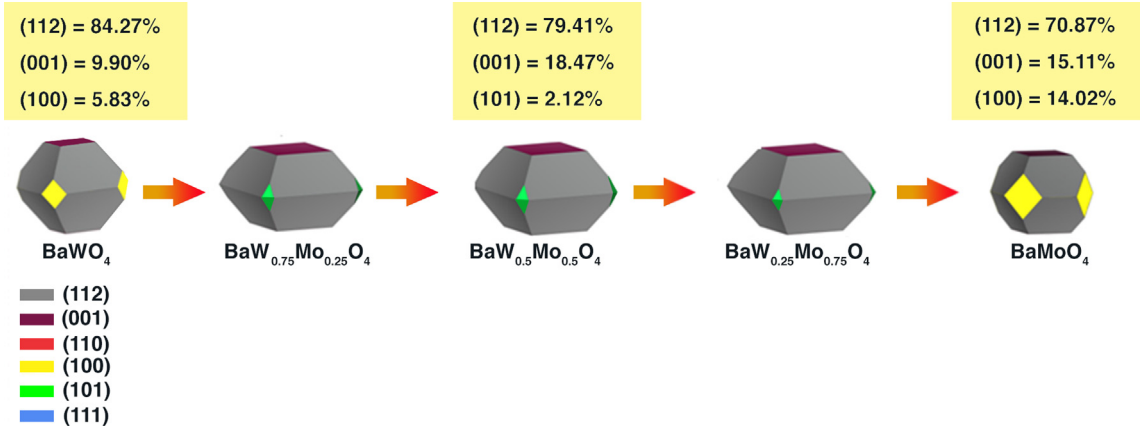

Fig. 8. Ideal morphologies of $BaW_{1-x}Mo_xO_4$ (x = 0, 0.25, 0.50, 0.75 and 1) solid solutions.

In order to describe the effects of the isoelectronic replacement of W^{6+} by Mo^{6+} on the morphology, the Wulff construction was applied to the intermediary composition of the $BaW_{1-x}Mo_xO_4$ solid solution. The ideal morphology of $BaW_{0.75}Mo_{0.25}O_4$ is based on 79.24% of (1 1 2), 18.72% (0 0 1), and 2.04% (1 0 1). The ideal morphology of $BaW_{0.50}Mo_{0.50}O_4$ involves 79.41% of (1 1 2), 18.47% (0 0 1), and 2.12% (1 0 1). Finally, 80.81% of (1 1 2), 17.91% (0 0 1), and 1.28% (1 0 1) constitute the ideal morphology for the $BaW_{0.25}Mo_{0.75}O_4$ system. These calculated morphologies for the $BaW_{1-x}Mo_xO_4$ system for x = 0, 0.25, 0.50, 0.75, and 1 are presented in Fig. 8.

In this study, the effect induced by the substitution in the $BaW_{1-x}Mo_xO_4$ solid solution is the alteration of the order of stability between the (0 0 1) and (1 1 2) crystal faces, as well as between the (1 0 0) and (1 1 0) crystal faces. This effect on the exposed crystal faces and relative surface energy values can be observed in Table 3.

Table 3 lists the values of the surface energies values obtained for the $BaW_{1-x}Mo_xO_4$ (x = 0, 0.25, 0.50, 0.75, and 1) solid solution, as well as the changes (increase or decrease) in surface energy for all the

Table 3
Surface energy values of the ideal morphology for the $BaW_{1-x}Mo_xO_4$ (x = 0, 0.25, 0.5, 075, and 1) solid solution. The values in parentheses indicate the increased/decreased surface energy with Mo content.

Surfaces	Surface energy (E_{surf})					
	$BaWO_4$	$BaW_{0.75}Mo_{0.25}O_4$	$BaW_{0.5}Mo_{0.5}O_4$	$BaW_{0.25}Mo_{0.75}O_4$	$BaMoO_4$	$\Delta Total_{(BMO-BWO)}$
(1 1 2)	0.92	0.65 (−0.27)	0.64 (−0.01)	0.63 (−0.01)	1.02 (+0.39)	(+0.10)
(0 0 1)	1.02	0.55 (−0.47)	0.54 (−0.01)	0.54 (0)	0.99 (+0.45)	(−0.03)
(1 1 0)	1.10	0.80 (−0.30)	0.79 (−0.01)	0.80 (+0.01)	1.23 (+0.43)	(+0.13)
(1 0 0)	1.22	1.08 (−0.14)	1.09 (+0.01)	1.09 (0)	1.17 (+0.08)	(−0.05)
(1 0 1)	1.31	0.91 (−0.40)	0.89 (−0.02)	0.90 (+0.01)	1.34 (+0.44)	(+0.03)
(1 1 1)	2.06	1.91 (−0.15)	1.89 (−0.02)	1.90 (+0.01)	2.23 (+0.33)	(+0.17)

compositions. From the analysis of the corresponding crystal faces, the order of stability of the $BaWO_4$ system is: (1 1 2) > (0 0 1) > (1 1 0) > (1 0 0) > (1 0 1) > (1 1 1); however, in the $BaW_{1-x}Mo_xO_4$ system, for x = 0.25, there is a different order of stability, as follows: (0 0 1) > (1 1 2) > (1 1 0) > (1 0 1) > (1 0 0) > (1 1 1), which is maintained for the other solid solutions at x = 0.50 and 0.75. This inversion in the (0 0 1) and (1 1 2) surface energy values, as well as those of (1 0 1) and (1 0 0), can be attributed to the presence of more Mo atoms in the system, as shown in Fig. 7. Thus, the morphology control and transformation mechanisms provide insights into the electronic, structural, and energetic properties.

In order to better understand the disappearance of the (1 1 2) crystal face in the experimental micrographs passing from x = 0.25 to 0.50 and 0.75, the morphologies of the $BaW_{1-x}Mo_xO_4$ (x = 0.25, 0.50, and 0.75) solid solution have been depicted in Fig. 9. The ideal morphology changes by tuning the values of E_{surf} of the different crystal faces, and a comparison between the theoretical and experimental morphologies for $BaW_{1-x}Mo_xO_4$ (x = 0.25, 0.50, 0.75) is presented at the top of Fig. 9.

Fig. 9 shows a schematic representation map of the morphologies of the $BaW_{1-x}Mo_xO_4$ (x = 0.25, 0.50, and 0.75) solid solution, in which the transformations are obtained by tuning the surface energies of the different crystal faces.

In this work, three ideal morphologies were considered (Fig. 9(a)), based on the results presented in Table 3, that indicate insignificant differences in surface energy values for the compositions x = 0.25, 0.50, and 0.75; therefore, we assume only an ideal morphology.

In order to obtain a morphology similar to that observed in the FE-SEM images, it is necessary to make a morphological modulation of the theoretical surface energies values. In this case, we started with the ideal morphology and by decreasing the value of (1 0 0) surface energy to 0.72 J/m^2, while simultaneously decreasing the corresponding value for (1 0 1) to 0.79 J/m^2, generating the shape *b*. The shapes *c* and *d* were created by decreasing the surface energy values of (1 0 1) to 0.74 and to 0.70 J/m^2, respectively. An increase in the (0 0 1) surface energy value to 1.10 J/m^2 and a simultaneous decrease in the (1 0 1) surface energy value to 0.77, 0.72, and 0.69 J/m^2 generates the shapes *e, f* and *g*, respectively.

Finally, the increase in the surface energy value to 1.50 and to 1.60 J/m^2 for (0 0 1) was simulated, simultaneously increasing the (1 1 2) surface energy value from 0.64 to 0.95, 0.89, and 0.86 J/m^2, as well as decreasing the energy value for (1 0 0) crystal face to 0.56 J/m^2, generates the shape *h*. An important objective of this study is to compare experimental and theoretical results and consider their differences in order to arrive at an understanding of the real system. The experimental micrographs display the images of the morphology in the real conditions, associated to the synthesis method employed. The variation of reaction conditions can produce different morphologies. From the theoretical side, the values of the E_{surf} are calculated *in vacuum*, i.e. the surrounding medium is not taken into account. Then, surface energy is not a constant material property and may depend on the environment in contact with the surface, such as the adsorption of a reactant, surfactant, or any species present in the solution, which can promote the

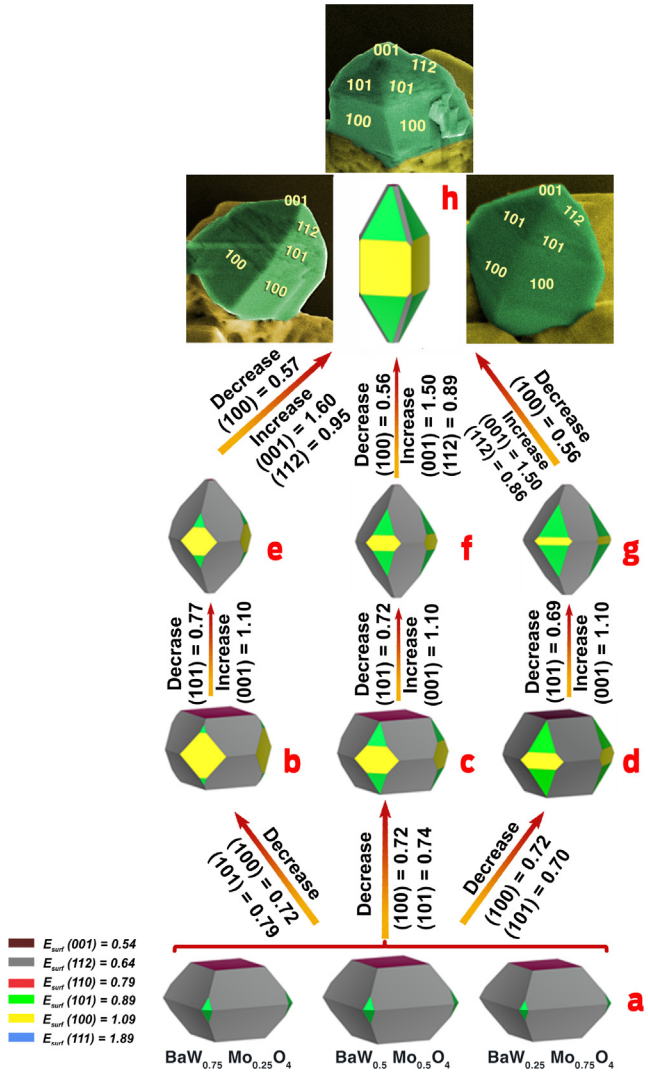

Fig. 9. Equilibrium shapes of $BaW_{1-x}Mo_xO4$ (x = 0.25, 0.50, 0.75) solid solutions via the Wulff construction principle. Experimental micrographs are also included for comparison purposes. Surface energy is in J m^{-2}.

stability of a particular surface, structure, or facet. In our case, the crystal faces (1 1 0) and (1 1 1) do not contribute to the experimental morphology; this means that these crystal faces are destabilized in the real conditions.

4. Conclusions

The formation of solid solutions $BaW_{1-x}Mo_xO_4$ (x = 0, 0.25, 0.5, 075, and 1) by using a simple co-precipitation method was reported for the first time, and their crystal structures and phase compositions were

experimentally determined, employing XRD with Rietveld refinements. FT-IR and MR spectroscopy, in combination with FE-SEM, were used to describe the microstructure and chemical composition of the synthesized materials. First-principles calculations were performed to obtain the relative stability of the (1 1 2), (0 0 1), (1 1 0), (1 0 1), (1 0 0), and (1 1 1) crystal faces, and Wulff construction was employed to rationalize the crystal morphologies observed in the FE-SEM images. This study is designed to serve as a roadmap of the available morphologies of the $BaW_{1-x}Mo_xO_4$ solid solutions (x = 0, 0.25, 0.5, 075, and 1) in order to understand the fundamentals, key advantages, and potential applications of the transformation processes along the synthesis pathway, where the experimental and theoretical morphologies of the $BaW_{1-x}Mo_xO_4$ solid solutions are well-matched. We showed that the substitution of W^{6+} by Mo^{6+} enhances the electron-transfer process due to a stronger Mo(4d)−O(2p) hybridization compared to W(5d)−O(2p) for the W/Mo−O superficial bonds; this is responsible for the change in morphology from $BaWO_4$ to $BaMoO_4$.

The synthetic approach and findings reported here are important for understanding the structure–property relationships of molybdate/tungstate compounds, which have potential applications in the design of novel functional materials.

Acknowledgments

The authors acknowledge the financial support from Universitat Jaume I, for project UJI-B2016-25, Generalitat Valenciana for PrometeoII/2014/022, Prometeo/2016/079, ACOMP/2014/270, ACOMP/2015/1202, Ministerio de Economia y Competitividad, project CTQ2015-65207-P, Fundação de Amparo à Pesquisa do Estado de São Paulo (FAPESP) (2013/07296-2). Programa de Cooperación Cientifica con Iberoamerica (Brasil) of Ministerio de Educación (PHBP14-00020). M.C. acknowledges Generalitat Valenciana for Santiago Grisolia Program 2015/033. We also wish to thank the Servei d'Informática, Universitat Jaume I, for their generous allocation of computer time. The important help of Enio Longo in the improvement of the final versions of the figures is recognized.

References

[1] D.A. Spassky, S.N. Ivanov, V.N. Kolobanov, V.V. Mikhailin, V.N. Zemskov, B.I. Zadneprovski, L.I. Potkin, Optical and luminescent properties of the lead and barium molybdates, Radiat. Meas. 38 (4–6) (2004) 607–610.
[2] J. Liu, J. Ma, B. Lin, Y. Ren, X. Jiang, J. Tao, X. Zhu, Room temperature synthesis and optical properties of $SrMoO_4$ crystallites by w/o microemulsion, Ceram. Inter. 34 (6) (2008) 1557–1560.
[3] T. Thongtem, S. Kungwankunakorn, B. Kuntalue, A. Phuruangrat, S. Thongtem, Luminescence and absorbance of highly crystalline $CaMoO_4$, $SrMoO_4$, $CaWO_4$ and $SrWO_4$ nanoparticles synthesized by co-precipitation method at room temperature, J. Alloy. Compd. 506 (1) (2010) 475–481.
[4] Y. Sun, J. Ma, J. Fang, C. Gao, Z. Liu, Photoluminescent improvement of $SrMoO_4$ by the electrochemical formation of Ca^{2+}-doped solid solutions, Inorg. Chem. Commun. 14 (8) (2011) 1221–1223.
[5] A.P.A. Marques, F.V. Motta, M.A. Cruz, J.A. Varela, E. Longo, I.L.V. Rosa, $BaMoO_4$:Tb^{3+} phosphor properties: Synthesis, characterization and photophysical studies, Solid State Ionics 202 (1) (2011) 54–59.
[6] M.C. Oliveira, L. Gracia, I.C. Nogueira, M.F.C. Gurgel, J.M.R. Mercury, E. Longo, J. Andrés, Synthesis and morphological transformation of $BaWO_4$ crystals: Experimental and theoretical insights, Ceram. Inter. 42 (2016) 10913–10921.
[7] L. Liu, S. Zhang, M.E. Bowden, J. Chaudhuri, J.J.D. Yoreo, In situ TEM and AFM investigation of morphological controls during the growth of single crystal $BaWO_4$, Cryst. Growth Des. 18 (3) (2018) 1367–1375.
[8] M.C. Oliveira, L. Gracia, I.A.C. Nogueira, M.F.C. Gurgel, J.M.R. Mercury, E. Longo, J. Andrés, On the morphology of $BaMoO_4$ crystals: A theoretical and experimental approach, Cryst. Res. Technol 51 (2016) 634–644.
[9] M.C. de Oliveira, T. Marinho, L. Gracia, E. Longo, J. Andrés, Analysis for the morphology prediction of materials from first principles calculations, in: J. Li, J. Li, Y. Chu (Eds.), Crystal Growth: Concepts, Mechanisms and Applications, Nova Science Publisher, Estados Unidos, 2017.
[10] C. Bouzidi, N. Sdiri, A. Boukhachem, H. Elhouichet, M. Férid, Impedance analysis of $BaMo_{1-x}W_xO4$ ceramics, Superlattice. Microst. 82 (Supplement C) (2015) 559–573.
[11] S. Vidya, S. Solomon, J.K. Thomas, Structral optical and dielectric characterization of nanocrystalline $AMo_{0.5}W_{0.5}O_4$ (where A = Ba, Sr and Ca) Prepared by Single Step Modified Combustion Technique, Mater. Today- Proc. 2 (3) (2015) 904–908.
[12] A. Sanchez-Martinez, O. Ceballos-Sanchez, C. Koop-Santa, E.R. López-Mena, E. Orozco-Guareño, M. García-Guaderrama, N-doped TiO_2 nanoparticles obtained by a facile coprecipitation method at low temperature, Ceram. Inter. 44 (5) (2018) 5273–5283.
[13] M. Ghaed-Amini, M. Bazarganipour, M. Salavati-Niasari, K. Saberyan, Morphology and photoluminescence of $BaMoO_4$ micro- and nano-crystals synthesized by co-precipitation method, Trans. Nonferrous Met. Soc. China 25 (12) (2015) 3967–3973.
[14] Z. Shahri, A. Sobhani, M. Salavati-Niasari, Controllable synthesis and characterization of cadmium molybdate octahedral nanocrystals by coprecipitation method, Mater. Res. Bull. 48 (10) (2013) 3901–3909.
[15] M.R. Ghazanfari, M. Kashefi, M.R. Jaafari, Optimizing and modeling of effective parameters on the structural and magnetic properties of Fe_3O_4 nanoparticles synthesized by coprecipitation technique using response surface methodology, J. Magn. Magn. Mater. 409 (2016) 134–142.
[16] J.C. Sczancoski, L.S. Cavalcante, N.L. Marana, R.O. da Silva, R.L. Tranquilin, M.R. Joya, P.S. Pizani, J.A. Varela, J.R. Sambrano, M. Siu Li, E. Longo, J. Andrés, Electronic structure and optical properties of $BaMoO_4$ powders, Curr. Appl. Phys. 10 (2) (2010) 614–624.
[17] H. Rietveld, A profile refinement method for nuclear and magnetic structures, J. Appl. Crystallogr. 2 (2) (1969) 65–71.
[18] A.C. Larson, R.B. Von Dreele, General structure analysis system (GSAS) program, Los Alamos, NM, Rep. N°. LAUR 86–748, Los Alamos National Laboratory, University of California, 2004.
[19] W. Finger, D.E. Cox, A.P. Jephcoat, A correction for powder diffraction peak asymmetry due to axial divergence, J. Appl. Crystallogr. 27 (1994) 892–900.
[20] P. Stephens, Phenomenological model of anisotropic peak broadening in powder diffraction, J. Appl. Crystallogr. 32 (2) (1999) 281–289.
[21] C.T. Lee, W.T. Yang, R.G. Parr, Development of the Colle-Salvetti correlation-energy formula into a functional of the electron density, Phys. Rev. B: Condens. Matter 37 (1988) 785–789.
[22] A.D. Becke, Density-functional thermochemistry. III. The role of exact exchange, J. Chem. Phys 98 (1993) 5648–5652.
[23] R. Dovesi, R. Orlando, A. Erba, C.M. Zicovich-Wilson, B. Civalleri, S. Casassa, L. Maschio, M. Ferrabone, M. De La Pierre, P. D'Arco, Y. Noël, M. Causà, M. Rérat, B. Kirtman, CRYSTAL14: A program for the ab initio investigation of crystalline solids, Int. J. Quantum Chem. 114 (19) (2014) 1287–1317.
[24] M.L. Moreira, J. Andrés, L. Gracia, A. Beltrán, L.A. Montoro, J.A. Varela, E. Longo, Quantum mechanical modeling of excited electronic states and their relationship to cathodoluminescence of $BaZrO_3$, J. Appl. Phys. 114 (2013) 043714.
[25] M.C. Oliveira, L. Gracia, M. de Assis, I.L.V. Rosa, M.F. do Carmo Gurgel, E. Longo, J. Andrés,, Mechanism of photoluminescence in intrinsically disordered $CaZrO_3$ crystals: First principles modeling of the excited electronic states, J. Alloy. Compd. 722 (Supplement C) (2017) 981–995.
[26] A. Beltrán, L. Gracia, E. Longo, J. Andrés, First-principles study of pressure-induced phase transitions and electronic properties of $Ag2MoO_4$, J. Phys. Chem. C 118 (2014) 3724–3732.
[27] M.T. Fabbro, C. Saliby, L.R. Rios, F.A.L. Porta, L.E. Gracia, M.S. Li, J. Andrés, L.P.S. Santos, E. Longo, Identifying and rationalizing the morphological, structural, and optical properties of B-Ag_2MoO_4 microcrystals, and the formation process of Ag nanoparticles on their surfaces: combining experimental data and first-principles calculations, Sci. Technol. Adv. Mater 16 (2015) 065002.
[28] L. Gracia, V.M. Longo, L.S. Cavalcante, A. Beltrán, W. Avansi, M.S. Li, V.R. Mastelaro, J.A. Varela, E. Longo, J. Andrés, Presence of excited electronic state in $CaWO_4$ crystals provoked by a tetrahedral distortion: An experimental and theoretical investigation, J. Appl. Phys. 110 (2011) 043501.
[29] F.M.C. Batista, F.A.L. Porta, L. Gracia, E. Cerdeiras, L. Mestres, M.S. Li, N.C. Batista, J. Andrés, E. Longo, L.S. Cavalcante, A joint experimental and theoretical study on the electronic structure and photoluminescence properties of $Al_2(WO_4)_3$ powders, J. Mol. Struct. 1081 (2015) 381–388.
[30] E. Longo, D.P. Volanti, V.M. Longo, L. Gracia, I.C. Nogueira, M.A.P. Almeida, A.N. Pinheiro, M.M. Ferrer, L.S. Cavalcante, J. Andrés, Toward an understanding of the growth of Ag filaments on α-Ag_2WO_4 and their photoluminescent properties: a combined experimental and theoretical study, J. Phys. Chem. C 118 (2014) 1229–1239.
[31] G.S. Silva, L. Gracia, M.T. Fabbro, L.P. Serejo dos Santos, H. Beltrán-Mir, E. Cordoncillo, E. Longo, J. Andrés, Theoretical and experimental insight on Ag_2CrO_4 microcrystals: synthesis, characterization, and photoluminescence properties, Inorg. Chem. 55 (17) (2016) 8961–8970.
[32] A.F. Gouveia, M.M. Ferrer, J.R. Sambrano, J. Andrés, E. Longo, Modeling the atomic-scale structure, stability, and morphological transformations in the tetragonal phase of $LaVO_4$, Chem. Phys. Lett. 660 (2016) 87–92.
[33] http://Www.Crystal.Unito.It/Basis_Sets/Molibdenum.Html.
[34] F. Cora, A. Patel, N.M. Harrison, R. Dovesi, C.R.A. Catlow, An Ab initio hartree-fock study of the cubic and tetragonal phases of bulk tungsten trioxide, J. Am. Chem. Soc. 118 (1996) 12174–12182.
[35] http://Www.Crystal.Unito.It/Basis_Sets/Oxygen.Html.
[36] http://Www.Tcm.Phy.Cam.Ac.Uk/Mdt26/Basis_Sets/Ba_Basis.Txt.
[37] H.J. Monkhorst, J.D. Pack, Special points for Brillouin-zone integrations, Phys. Rev. B 13 (12) (1976) 5188.
[38] G. Wulff, Xxv. zur frage der geschwindigkeit des wachsthums und der auflösung der krystallflächen, Z. Krist.-Cryst. Mater. 34 (1) (1901) 449–530.
[39] D. Errandonea, J. Pellicer-Porres, F.J. Manjón, A. Segura, C. Ferrer-Roca, R.S. Kumar, O. Tschauner, J. López-Solano, P. Rodríguez-Hernández, S. Radescu, A. Mujica, A. Muñoz, G. Aquilanti, Determination of the high-pressure crystal structure of $BaWO_4$ and $PbWO_4$, Phys. Rev. B 73 (22) (2006) 224103.
[40] T.T. Basiev, A.A. Sobol, Y.K. Voronko, P.G. Zverev, Spontaneous Raman

spectroscopy of tungstate and molybdate crystals for Raman lasers, Opt. Mater. 15 (3) (2000) 205–216.
[41] K. Nakamoto, Infrared and Raman Spectra of Inorganic and Coordination Compounds, 4th ed., Wiley, New York, 1986.
[42] S. Vidya, S. Solomon, J.K. Thomas, Structral optical and dielectric characterization of nanocrystalline $AMo_{0.5}W_{0.5}O_4$ (where A = Ba, Sr and Ca) prepared by single step modified combustion technique, Mater. Today: Proc. 2 (3) (2015) 904–908.
[43] J.B. Foresman, E. Frisch, Exploring Chemistry with Electronic Structure Methods, Frequency Calculations. Gaussian, Inc., Pittsburgh. P.A, 1996, pp. 61–90.
[44] M. Li, Y. Guan, Y. Yin, X. Cui, S. Rong, G. Jin, Y. Hao, Q. Wu, Controllable synthesis of 3D $BaXO_4$ (X = W, Mo) microstructures by adjusting nucleation stage and their photoluminescence properties, Superlattice Microst. 80 (Supplement C) (2015) 222–228.
[45] A. Phuruangrat, T. Thongtem, S. Thongtem, Precipitate synthesis of $BaMoO_4$ and $BaWO_4$ nanoparticles at room temperature and their photoluminescence properties, Superlattices Microstruct. 52 (1) (2012) 78–83.
[46] T. Thongtem, A. Phuruangrat, S. Thongtem, Characterization of $MMoO_4$ (M = Ba, Sr and Ca) with different morphologies prepared using a cyclic microwave radiation, Mater. Lett. 62 (3) (2008) 454–457.
[47] T. Thongtem, A. Phuruangrat, S. Thongtem, Synthesis of $CaWO_4$, $SrWO_4$ and $BaWO_4$ with nanosized particles using cyclic microwave radiation, J. Ceram. Process. Res. 9 (3) (2008) 258–261.
[48] Z.Y. Gao, W. Sun, Y.H. Hu, X.-W. Liu, Surface energies and appearances of commonly exposed surfaces of scheelite crystal, T. Nonferr. Metal. Soc 23 (2013) 2147–2152.